HEAT TRANSFER AND FRICTION FACTOR OF FLAT PLATE SOLAR COLLECTOR WITH Al_2O_3-CuO/WATER HYBRID NANOFLUIDS: EXPERIMENTAL AND ANN PREDICTIONS

UDC:621.311.243
Original scientific paper https://doi.org/10.46793/aeletters.2025.10.1.1

Solomon Mesfin[1,2], Veeredhi Vasudeva Rao[2], L. Syam Sundar[*3], Kotturu V.V. Chandra Mouli[4]

[1]Department of Mechanical Engineering, University of Gondar, Gondar, Ethiopia
[2]Department of Mechanical, Bioresources and Biomedical Engineering, School of Engineering, CSET, University of South Africa (UNISA), South Africa
[3]Department of Mechanical Engineering, College of Engineering, Prince Mohammad Bin Fahd University, Al-Khobar, 31952, Saudi Arabia
[4]Department of Mechanical and Industrial Engineering, College of Engineering, Majmaah University, Al-Majmaah, 11952, Saudi Arabia

Abstract:
The Nusselt number, heat transfer, and friction factor of flat plate collector working with Al_2O_3-CuO/water hybrid nanofluids were estimated experimentally, and the obtained data is used for the artificial neural network- Support Vector Regression method. Experiments were conducted from 09:00 to 16:30 hr, with volume loadings of 0.048%, 0.096%, 0.144%, 0.192% and 0.24%, respectively. The entire region is divided into time zone 1 (09:00 hr to 13:00 hr) and time zone 2 (13:00 hr to 16:30 hr). Results show the time zone-1, at 13:00 hrs, at 0.24% vol. and a Reynolds number of 364.66, the Nusselt number is enhanced by 20.43%, and at time zone-2, at 16:30 hrs, at 0.24% vol., and at Reynolds number of 211.23, the Nusselt number is enhanced by 14.08%, respectively, over the base fluid. Similarly, for time zone-1 and time zone-2, at 13:00 hrs and 16:30 hrs, at 0.24% vol. and at Reynolds number 364.66 and 211.23, the friction factor is enhanced by 15.34% and 11.50%, respectively, over the base fluid. The employed support vector regression algorithm accurately predicts the values with experimental data. The correlation coefficients found for the Nusselt number, heat transfer, and friction factor are 0.99497, 0.9947, and 0.99955, respectively.

ARTICLE HISTORY
Received: 15 August 2024
Revised: 2 October 2024
Accepted: 10 October 2024
Published: 31 March 2025

KEYWORDS
Flat plate solar collector, Heat transfer coefficient, Friction factor, Nusselt number, Enhancement, Hybrid nanofluids, ANN analysis

1. INTRODUCTION

Solar energy, derived from the sun, is the primary source of many forms of renewable energy. The annual solar energy received by the Earth is 3,400,000 EJ, the total solar flux reaching the Earth is 1.08×10^8 GW, and the solar constant at the Earth's distance from the sun is 1367 W/m^2. This sustainable energy source can be utilised for the generation of electricity as well as for the heating of water; sun photovoltaic cells can directly harness power from sun energy. Similarly, solar collectors can be used to directly obtain hot water from solar energy. Solar collectors are devices that transform solar radiation into thermal energy. The global thermal energy conversion achieved by solar collectors at the end of 2013 was around 37 GWh, corresponding to a total area of 53.5 × 107 m^2 [1].

The solar collectors are of the flat plate variety, characterised by their uncomplicated design, cost-

*CONTACT: L. Syam Sundar, email: sslingala@gmail.com

effectiveness, and ease of operation. Due to its superior benefits compared to other collectors, these collectors are commonly utilised for home and industrial purposes. The flat plate collector (FPC) captures solar energy and turns it into thermal energy by transferring it through a working fluid, such as water (w), ethylene glycol (EG), and propylene glycol (PG) [2,3]. The FPC system utilises an absorber plate of either aluminium or copper coated with a highly efficient selective coating to maximise solar energy absorption. Replacing poor thermal conductivity fluids with high thermal conductivity nanofluids can boost the collector heat transfer rates. The notion of nanofluids was first found by Choi [4], who introduced the dispersion of solid particles of nanometre dimensions into a base fluid.

The preliminary research on FPC involved using mono nanofluids, which are single nanofluids. Ziyadanogullari et al. [5] employed nanofluids consisting of Al_2O_3/water, CuO/water, and TiO_2/water in FPC and achieved improved collector efficiency. In their study, Sundar et al. [6] examined using Al_2O_3/water nanofluid in FPC. They achieved a collector efficiency of 76% when the nanofluid concentration (ϕ) was 0.3%, and the mass flow rate was 0.083 kg/sec. Rajput et al. [7] employed Al_2O_3/water in FPC and observed a collector efficiency of 21.32% when the concentration of Al_2O_3 was 0.3% and the volume flow rate was 1.3 L/min. Hawwash et al. [8] utilised Al_2O_3/water nanofluid in FPC and demonstrated a 16.67% improvement in collector efficiency. Jouybari et al. [9] discovered that the collector efficiency of SiO_2/water nanofluids in a FPC was 73% when the volume flow rate was 1.5 L/min, and the concentration of SiO_2 was 0.6%. Kiliç et al. [10] discovered that the collector efficiency of a FPC can reach 48.67% when employing a nanofluid made of TiO_2 nanoparticles dispersed in water at a concentration of 2 wt%. Said et al. [11] utilised TiO_2-water nanofluids in FPC and achieved an improved thermal efficiency of the collector.

Hybrid nanoparticles are formed when two or more nanoparticles mix with each other. The hybrid nanofluids exhibit enhanced synergistic features, namely in terms of thermal conductivity and viscosity, compared to nanofluids based only on single nanoparticles. The use of hybrid nanofluids in FPC and their ability to improve heat transfer rates. Okonkwo et al. [12] employed a hybrid nanofluid consisting of Al_2O_3-iron and water in FPC. They observed a collector efficiency of 1.79% when the volume fraction (ϕ) of the nanofluid was 0.1%. Verma et al. [13] employed CuO-MWCNT/water and MgO-MWCNT/water hybrid nanofluids in FPC and observed that the MgO-MWCNT/water hybrid nanofluid exhibited greater exergetic efficiency (71.54%) and energy efficiency (70.55%). Saleh and Sundar [14] employed a hybrid nanofluid consisting of MWCNT+Fe_3O_4 in water for FPC. They achieved a 28.09% improvement in collector efficiency and enhancements of 39.23% in heat transfer coefficient and 18.98% in friction factor at a concentration of 0.3% and a Reynolds number of 1413. In their study, Sundar et al. [15] utilised a hybrid nanofluid consisting of ND-Co_3O_4 and water in an FPC system. They found that this nanofluid led to a 22.91% improvement in collector efficiency and enhancements of 21.23% in the Nusselt number and 13.2% in the friction factor. These improvements were obtained at a concentration of 0.15 wt% and a volume flow rate of 1.35 L/min. Elsherbiny et al. [16] observed a maximum PEC of 1.845 using Al_2O_3-ZnO-Ag hybrid nanofluids in microchannel heat sinks. Elsherbiny et al. [17] explained the miniature nanofluids technology for heat transfer enhancement in micro-cooling based on a review study.

Ajeena et al. [18] observe thermal and exergy efficiencies of FPSC enhanced by 26.2% and 16.05% with ZrO_2-SiC/DW hybrid nanofluid. Alfellag et al. [19] prepared 20:80, 40:60, 50:50, 60:40, and 80:20 (CT-MWCNTs:TiO_2)/water nanofluids and found 60:40 based hybrid nanofluids showing high thermophysical performance factor compared to other ratios. Selvam et al. [20] observed thermal and exergy efficiency of 72.8% and 22.9%, a heat transfer coefficient of 133.2 W/m^2K, and a Coefficient of Performance of 7.9 by using Al_2O_3/Ni/water nanofluids in an FPC. Sathish et al. [21] observed 70.4% of thermal efficiency by using Al_2O_3, Cu, MWCNT, SiO_2 blended nanofluids in a solar flat plate collector.

Using artificial neural networks (ANNs) to predict experimental results would improve data precision and save time consumption. The ANN facilitate the process of curve fitting and the creation of new correlations. Therefore, most researchers today consider ANN to be the ideal option for assessing their experimental data. This document provides a study on the utilisation of nanofluids in FPC with ANN is presented here. Xu et al. [22] employed various ANN models, such as LS-SVR and ANFIS, to analyse the experimental data of Al_2O_3/water nanofluids in FPC. They observed an average fluctuation of 2.772%, a mean squared error (MSE) of 0.000392, and a coefficient of determination (R^2) of 0.99312 between the experimental and ANN data. Mirzaei and Mohiabadi [23] utilised an Artificial Neural Network (ANN) to analyse the data of water-mixed CuO and Al_2O_3 in FPC. The results showed a difference of ±2.0% between the experimental and ANN data.

Zhang et al. [24] employed the ANN-Lavenberg-Marquadt model to analyse the rGO/water data in FPC. The study revealed a perfect alignment between the experimental data and the ANN data. In their study, Sadeghzadeh et al. [25] employed the ANN-MLP and ANN-RBF models to analyse the experimental data of TiO_2/water in FPC. They observed that the ANN-MLP model exhibited higher accuracy in its predictions compared to the ANN-RBF model. Bahiraei et al. [26] have explained the importance of Artificial Intelligence (AI) algorithms for thermal systems in their review paper. Tomy et al. [27] utilised artificial neural networks (ANN) to analyse the experimental data of Ag/water nanofluids in FPC. They observed a high level of accuracy, with a difference of only ±2.0% between the experimental and ANN data.

Upon analysing the data, the research has determined that there is a lack of information regarding heat transfer and friction factor data in relation to the use of Al_2O_3-CuO hybrid nanofluid in FPC. Additionally, there is no available data on the predictions made by the ANN-support vector regression model for the same hybrid nanofluids. The study focused on the development and utilization of uniform water mixed nanofluids to evaluate their thermophysical properties and thermal efficiency. Additionally, the study examined the flow of Al_2O_3-CuO hybrid nanofluid in FPC under thermosyphon conditions.

2. MATERIAL AND METHODS

2.1. Preparation of Hybrid Nanofluids

The hybrid nanofluids were prepared by adding nanoparticles into water. Table 1 is the physical properties of Al_2O_3, CuO and water, respectively.

Since, there is no standard procedure to select the mixing ratio of Al_2O_3, and CuO nanoparticles in the literature, hence the equal ratio (50:50%) of Al_2O_3, and CuO nanoparticles were considered for the preparation of Al_2O_3-CuO hybrid nanofluids. The weight of Al_2O_3, and CuO nanoparticles required is estimated from Eq. (1).

$$\text{Vol. concentration, } \phi \times 100 = \frac{\left[\frac{W_{np}}{\rho_{np}}\right]}{\left[\frac{W_{np}}{\rho_{np}}\right]+\left[\frac{W_{bf}}{\rho_{bf}}\right]} \quad (1)$$

where: ϕ is volume concentration (%), W_{np} is the weight of nanoparticles (Al_2O_3 and CuO) (g), W_{bf} is the weight of base fluid, ρ_{np} is the density of nanoparticles (Al_2O_3 is 3990 kg/m^3, CuO is 6310 kg/m^3), and ρ_{bf} is density of base fluid (1000 kg/m^3).

Since a 50:50% of Al_2O_3 and CuO nanoparticles were used in this study, hence 4 L of water-based Al_2O_3 nanofluids were prepared and kept separately, and then another 4 L of water-based CuO nanofluids were prepared and kept separately, later both nanofluids were mixed together in a large quantity tank with mechanical stirrer in order to get hybrid nanofluids. Table 2 indicates the weights of Al_2O_3 and CuO nanoparticles required for 4 L of water for the preparation of various nanofluids.

Since there is no standard rule to choose the specific volume concentrations of nanofluids in the open literature, even in the published papers also researchers have chosen their own volume concentrations. In general, there is an agglomeration problem for higher particle volume concentrations in the base fluid, creating clogging in test setup. So, to avoid such agglomeration problems, we have chosen very low particle volume concentrations. Moreover, the cost of the nanoparticles also matters for the preparation of large-volume concentrations of nanofluids. For large-volume concentrations, a large quantity of nanoparticles is required, and we need to spend lots of money.

In order to prepare the 0.048% vol. of water-based Al_2O3 nanofluid, 7.68 g of Al_2O_3 nanoparticles were dispersed in 4 L of water and then stirred with a mechanical stirrer for about 3 hrs at 300 rpm. Later, another nanofluid of 0.096%, 0.144%, 0.192%, and 0.24% vol. were prepared by dispersing 15.37, 23.07, 30.78, 38.49 g of Al_2O_3 nanoparticles into 4 L of water and then stirred with mechanical stirrer for 3 hrs at 300 rpm.

Similarly, for the preparation of 0.048% vol. of water-based CuO nanofluid, 12.15 g of CuO nanoparticles were dispersed in 4 L of water and then stirred with a mechanical stirrer for about 3 hrs at 300 rpm. Later, another nanofluid of 0.096%, 0.144%, 0.192%, and 0.24% vol. were prepared by dispersing 24.31, 36.49, 48.68, 60.87 g of CuO nanoparticles into 4 L of water and then stirred with a mechanical stirrer for 3 hrs at 300 rpm.

Later, the same Al_2O_3 and CuO nanofluids concentrations were mixed with a mechanical stirrer for about 3 hrs at 300 rpm. The prepared hybrid nanofluids are indicated in Fig. 1.

A stability test is required to understand whether the nanoparticles are uniformly dispersed in base fluids. The stability of the nanoparticles in the base fluid is expressed in terms of its zeta potential value. The homogeneity of the created Al_2O_3-CuO/water hybrid nanofluids was examined with a ZetaSizer Nano ZS instrument (Malvern Instruments, USA). The gadget utilises the dynamic light scattering (DLS) technology. A cuvette is filled with 2 ml of hybrid nanofluid before being inserted into the equipment. The Zeta potential can demonstrate the homogeneity of nanofluids. If the zeta potential of manufactured nanofluids is 30 mV or lower, they are classified as stable nanofluids. The prepared hybrid nanofluids result in repulsive interactions between them. As a result, the Al_2O_3-CuO disperse evenly throughout the base fluid. According to the data, the zeta potential values for the loadings of 0.048%, 0.096%, 0.144%, 0.192%, and 0.24% are -42.3, -42.1, -41.4, 40.2, and -39.6 mV, respectively. The relationship between the zeta potential of particles and volume loadings is widely recognised. When the volume loading of the base fluid increases, the repulsive forces gradually decrease.

Fig. 1. Prepared hybrid nanofluids

Table 1. The physical properties of Al_2O_3, and CuO nanoparticles

	Density, kg/m^3	C_p, (J/kgK)	k, (W/mK)	Color	Diam. (nm)
Al_2O_3	3990	785.2	30	White	50
CuO	6310	540	33	Black	27
Water	1000	4179	0.613	---	----

Table 2. Required weights of CuO and Al_2O_3 nanoparticles for the known volume loadings

	Particle volume loading, ϕ (%)				
	0.048%	0.096%	0.144%	0.192%	0.24%
CuO	12.15g	24.31g	36.49g	48.68g	76.98g
Al_2O_3	7.68g	15.37g	23.07g	30.78g	38.49g
Al_2O_3-CuO,	19.83g	39.68g	59.56g	79.46g	99.36g
Water (L)	8 L	8 L	8 L	8 L	8 L

2.2. Experimental Setup

A flat plate collector is a device used to collect and absorb solar energy. Fig. 2(a) is the schematic diagram, and Fig. 2(b) is a photograph of an experimental setup used for water and hybrid nanofluids. The parts used are: (1) heat exchanger tank, (2) pump, (3) flow control valve, (4) flowmeter, (5) inlet temperature, (6) glass cover, (7) outlet temperature, (8) by-pass valve, (9) frame, (10) cold water tank, (11) cold water inlet, (12) cold water outlet, and (13) cold water supporter. The thermal efficiency of the collector is then calculated. The solar collector was positioned at Gondar, a town in Ethiopia situated at a latitude of 12.6˚ N and a longitude of 37.47˚ E in the northern hemisphere.

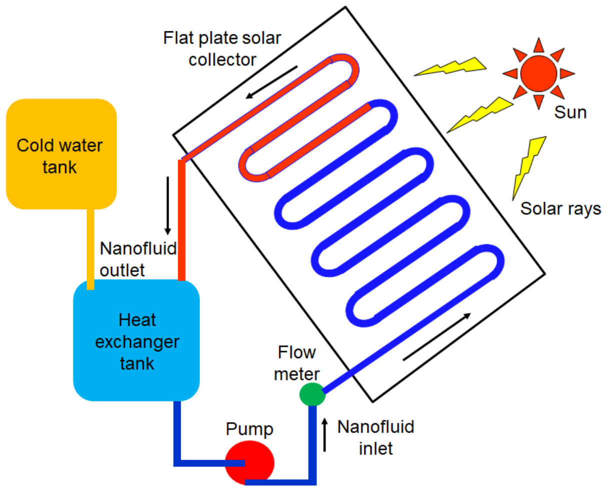

Fig. 2(a). Schematic diagram of an experimental setup

The town is elevated at 2133 meters above sea level. The flat plate solar collector was mounted at a tilt angle of 27.6˚ to maximise the amount of gathered radiation. The setup primarily includes an absorber plate for absorbing solar radiation, a single glass cover for minimising heat loss, a serpentine tube (inner diameter of 0.006 m, outer diameter of 0.007 m, and length of 5 m) for fluid circulation through the solar collector, a storage tank for storing working fluids and serving as a heat exchanger, a pump for delivering the fluid to the serpentine pipes, a bypass valve for redirecting fluids after adjusting the control valve, adjustable valves for controlling the flow rate in the main flow loop and bypass line, a flow meter for measuring fluid flow rate, a cold water storage tank, a table for supporting the water tank, and collector support for holding the flat plate solar collector. During the experimental test, the temperatures of the glass and plate, as well as the inlet and exit temperatures and mass flow rates of the working fluids, are measured to determine the thermal efficiency of the flat plate solar collector. The experiments were conducted from 09:00 to 16:30, with volume loadings of 0.048%, 0.096%, 0.144%, 0.192% and 0.24%, respectively. The time between 09:00 to 16:30 is divided into time zone-1 (09:00 to 13:00 hr) and time zone-2 (13:00 to 16:30 hr). The mass flow rate for time zone 1 varied from 0.56 to 1.36 L/min, and the mass flow rate for time zone 2 varied from 1.24 to 0.782 L/min.

The Nusselt number and friction factor of working fluid is given by Sundar et al. [15].

$$Q = \dot{m}\, C_p(T_o - T_i) = U_o A_o (T_s - T_m) \tag{2}$$

$$\frac{1}{U_o A_o} = \frac{1}{h_i A_i} + \frac{\ln\left(\frac{d_o}{d_i}\right)}{2\pi k L} \tag{3}$$

where: Q is rate of heat flow (W), $\dot{m}$ is mass flow rate (kg/s), C_p is specific heat (J/kg K), U_o is the overall heat exchanger (W/m^2), A_o is area (m^2), and T is the temperature (^{o}C), suffixes, 'o' is outlet, 'I' is inlet, 's' is surface, and 'm' is mean. The h_i is heat transfer coefficient (W/m^{2}K), k is thermal conductivity (W/mK), and L is length (m).

Fig. 2(b). Photograph of an experimental setup

Through Eqns. (2) and (3), the h_i is obtained [15].

$$Nu = \frac{h_i d_i}{k} \tag{4}$$

$$Re = \frac{4\dot{m}}{\pi d \mu} \tag{5}$$

where: Nu is Nusselt number, Re is Reynolds number, and d is diameter (m).

The factor in friction was estimated by [28],

$$f_{exp} = \frac{(\Delta P)}{\left(\frac{L}{d}\right)\left(\frac{\rho v^2}{2}\right)} \tag{6}$$

where: ΔP is pressure drop (Pas), v is velocity (m/sec).

2.3. ANN- Support Vector Regression (SVR)

Vapnik [29] have proposed the machine learning method known as SVR. The flow diagram of the SVR model is mentioned in Fig. 3. The SVR is a statistical technique that employs the notion of minimum risk of the structure and reduces the upper limit general error as opposed to the neural network's approach of minimising prediction error on training data. This model was first considered for solving the classification problems and then considered for prediction problems by establishing the Vapnik ε-insensitive function (Cortes, and Vapnik, [30]).

In SVR, the function $f(x)$ computes with the relation of inputs $X = \{x_1, x_2, x_3 \ldots\ldots x_n\}$ and targets $Y = \{y_1, y_2, y_3 \ldots\ldots y_n\}$, where $x_i \in R^n$, $y_i \in R$. Similar to this, because the cost function for creating the model rejects any training data that is close to the model prediction, the model created by SVR only depends on a subset of the training data. Suykens and Vandewalle [31] have presented the least-squares support vector machine, a different SVR variant.

Training of the SVR is as follows:

$$\text{minimize } \frac{1}{2}\|w\|^2 \tag{7}$$

$$\text{subject to } |y_i - \langle w, x_i \rangle - b| \le \varepsilon \tag{8}$$

where: x_i is a training sample with target value y_i. The values, $\langle w, x_i \rangle + b$ is the prediction, and ε is a free parameter.

The discrepancy between the experimental and anticipated values should be as small as possible in a suitable network. In general, the RMSE, which is shown in Eq. (9), is used to define performance.

$$RMSE = \sqrt{\frac{1}{n}\sum_i^n \left(C_{p,pr} - C_{p,ex}\right)^2} \tag{9}$$

$$R = \sqrt{1 - \frac{\sum_{i=1}^{n}\left(C_{p,\mathrm{ex}\,(i)} - C_{p,pr}\right)^2}{\frac{1}{N}\sum_{i=1}^{n}\left(C_{p,\mathrm{ex}\,(i)}\right)^2}} \qquad (10)$$

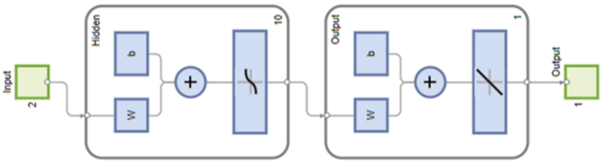

Fig. 3. The flow diagram of the SVR model

3. RESULTS AND DISCUSSION

3.1. Nusselt Number

Water and hybrid nanofluids' fixed mass flow rates were used to flow water and nanofluids in the FPC. The mass flow rate was adjusted with a pump. Every 30 minutes, the flow rate was a little increased. The mass flow rate varies from 0.56 to 1.35 L/min for time zone 1 and from 1.24 to 0.782 L/min for time zone 2. Two regions, commonly referred to as time zone-1 (09:00 hr to 13:00 hr) and time zone-2 (13:00 to 16:30), are separated by this nature. The mass flow rate is converted into Reynolds number (Re) through the Eq. (5).

The range of Re for water is 195 < Re < 470.18, for 0.048% vol. is 176.93 < Re < 426.52, for 0.096% vol. is 170.83 < Re < 411.82, for 0.144% vol. is 163.77 < Re < 394.8, for 0.192% vol. is 158.53 < Re < 382.17; for 0.24% vol. is 151.27 < Re < 364.66, respectively for time zone-1.

The range of Re for water is 431.87 < Re < 272.36, for 0.048% vol. is 391.77 < Re < 247.07, for 0.096% vol. is 378.26 < Re < 238.55, for 0.144% vol. is 362.63 < Re < 228.69, for 0.192% vol. is 351.03 < Re < 221.37, for 0.24% vol. is 334.95 < Re < 211.23, respectively for time zone-2.

Fig. 4 is the Nusselt number versus daytime. As it is observed, the Nusselt number increases with daytime. For the entire day, from 09:00 hr to 13:00 hr, the Nusselt number of nanofluids is increased and then from 13:30 hr to 16:30 hr, the Nusselt number is decreased. The Nusselt number (Nu) of hybrid nanofluids was evaluated in time zone-1 using Eq. (4), and the findings were presented in Fig. 5. The Nusselt number is greater for nanofluids compared to the base fluid at the same Reynolds numbers. As particles in a fluid rise, the Reynolds number lowers. This can be controlled by adjusting the flow rate and adding the viscosity of nanofluids. The Nusselt number in water increases with higher particle loadings and with higher Reynolds numbers. The Nu values are raised to 3.56%, 5.14%, 7.11%, 9.86%, and 11.05% when the particle loadings are 0.048%, 0.096%, 0.144%, 0.192%, and 0.24%. Additionally, the Nu values are further increased to 7.99%, 11.63%, 14.97%, 17.70%, and 20.43% at Re values of 151.27 and 364.66 over water. The primary cause for achieving larger Nusselt numbers is the increased value of k_{nf}. Increased particle loadings result in enhanced fluid-particle interaction, leading to elevated heat transfer rates. The fluid's exit temperature increased as the solar intensity gradually rose compared to the daytime, causing it to absorb more heat.

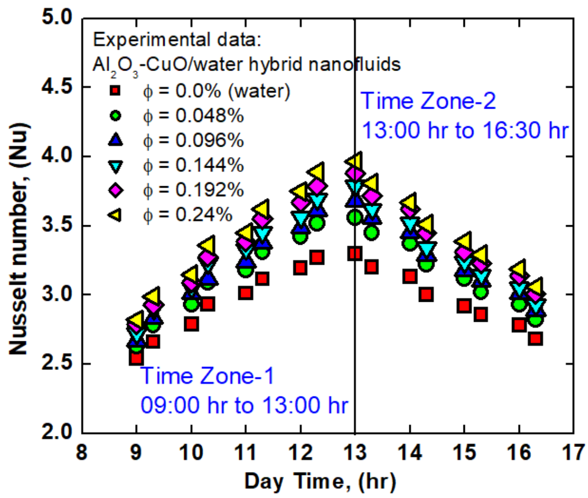

Fig. 4. Nusselt number versus day time

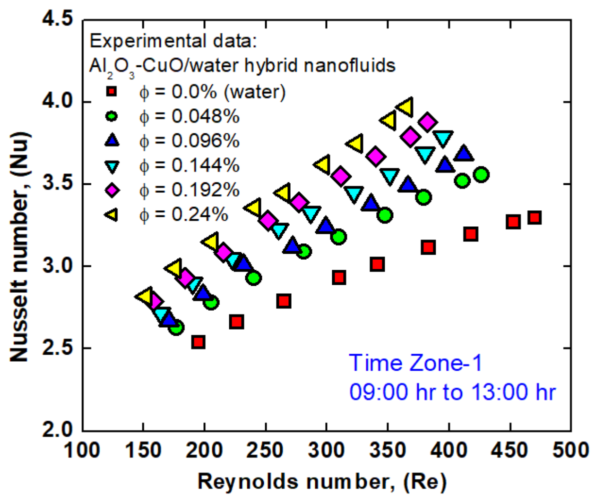

Fig. 5. Nusselt number versus Reynolds number for time zone-1

The analysis of the *Nu* of hybrid nanofluids for time zone-2 is conducted using Eq. (4), and the findings are presented in Fig. 6. In time zone-2, the Reynolds number declined as a result of a decrease in the mass flow rate of the working fluids, which was caused by a reduction in solar radiation. The Nusselt number increases with higher particle loadings in the water and decreases with lower Reynolds numbers. The Nu values increase by 7.77%, 11.21%, 13.08%, 16.20%, and 19.02% when the particle loadings are 0.048%, 0.096%, 0.144%, 0.192%, and 0.24%, respectively, compared to water. In addition, the *Nu* values decrease to 5.14%, 7.74%, 9.24%, 12.22%, and 14.08% when the Re values are 334.95 and 211.23, respectively.

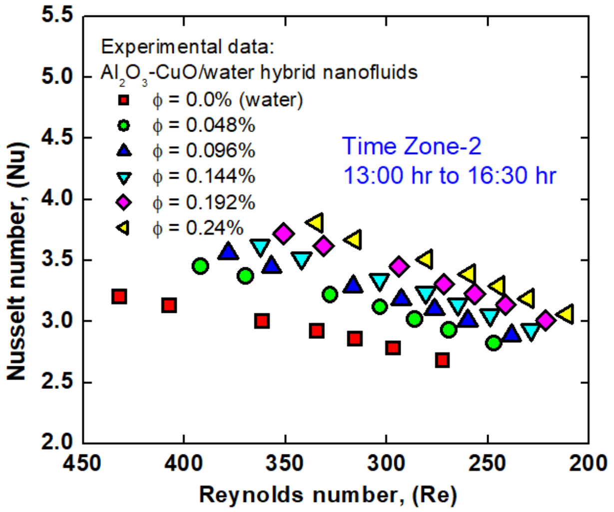

Fig. 6. Nusselt number versus Reynolds number for time zone-2

3.2. Heat Transfer Coefficient

The heat transfer coefficient of hybrid nanofluids was evaluated in time zone-1 using Eq. (3), and the findings were presented in Fig. 7. The heat transfer coefficient of nanofluids was increased with higher particle loadings and also increased with higher Reynolds numbers. The heat transfer coefficient values are raised to 4.77%, 7.41%, 11.91%, 16.62%, and 20.27% when the particle loadings are 0.048%, 0.096%, 0.144%, 0.192%, and 0.24%. The heat transfer coefficient values are further increased to 9.25%, 14.04%, 20.12%, 24.93%, and 30.43% at Re values of 151.27 and 364.66 over water.

The analysis of the heat transfer coefficient of hybrid nanofluids for time zone-2 is conducted using Eq. (3), and the findings are presented in Fig. 8. In time zone-2, the Reynolds number declined as a result of a decrease in the mass flow rate of the working fluids, which was caused by a reduction in solar radiation. The heat transfer coefficient values increase by 9.02%, 13.61%, 18.15%, 23.35%, and 28.9% when the particle loadings are 0.048%, 0.096%, 0.144%, 0.192%, and 0.24%, respectively, compared to water. In addition, the heat transfer coefficient values decreased to 6.36%, 10.07%, 14.14%, 19.12%, and 23.56% when the Re values were 334.95 and 211.23, respectively.

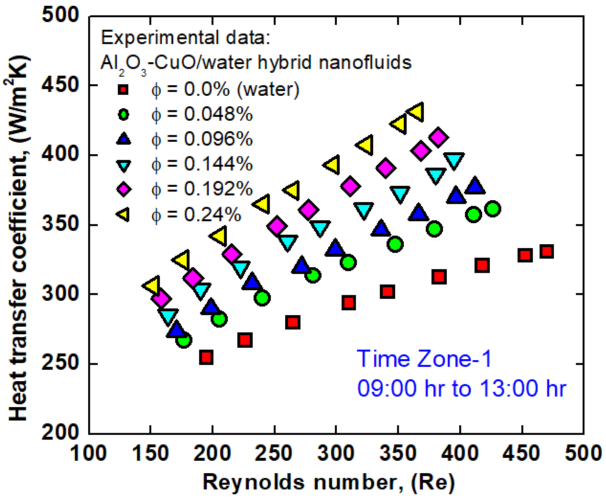

Fig. 7. Heat transfer coefficient versus Reynolds number for time zone-1

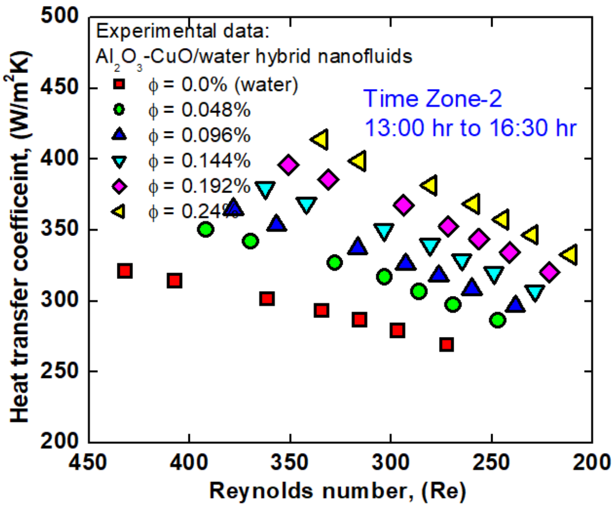

Fig. 8. Heat transfer coefficient versus Reynolds number for time zone-2

3.3. Friction Factor

The friction factor of hybrid nanofluids was evaluated in time zone-1 using Eq. (6), and the findings were presented in Fig. 9. The friction factor of nanofluids increased with higher particle loadings and also increased with higher Reynolds numbers. The friction factor values are raised to 3.01%, 5.14%, 6.05%, 8.19%, and 8.80% when the particle loadings are 0.048%, 0.096%, 0.144%, 0.192%, and 0.24%. The friction factor values are further increased to 7.26%, 10.93%, 12.4%, 14.61%, and 15.34% at Re values of 151.27 and 364.66 over water.

The analysis of the friction factor of hybrid nanofluids for time zone-2 is conducted using Eq. (6), and the findings are presented in Fig. 10. In time zone-2, the Reynolds number declined as a result of a decrease in the mass flow rate of the working fluids. The friction factor values increase by 5.94%, 8.64%, 12.02%, 13.37%, and 14.72% when the particle loadings are 0.048%, 0.096%, 0.144%, 0.192%, and 0.24%, respectively, compared to water. In addition, the friction factor values decreased to 3.41%, 6.39%, 8.94%, 10.22%, and 11.50% when the Re values were 334.95 and 211.23, respectively.

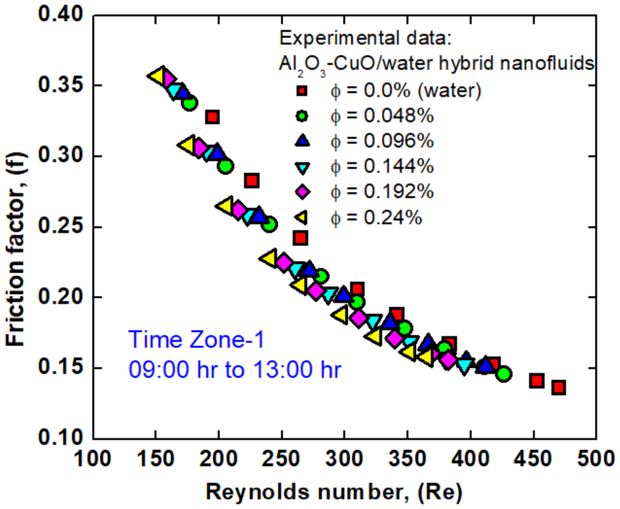

Fig. 9. Friction factor versus Reynolds number for time zone-1

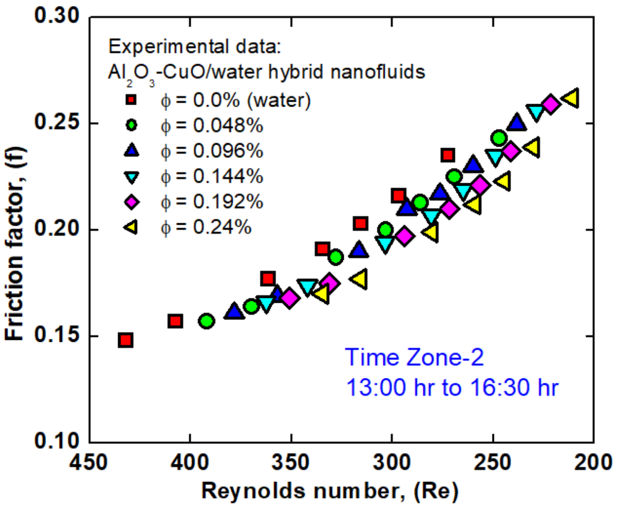

Fig. 10. Friction factor versus Reynolds number for time zone-2

Based on the experimental data, Nusselt number regression equations are proposed for two time zones.

Time zone-1:

$$Nu = 2.089 + 1.0028Re - 0.2731\phi + 0.011Re\phi \quad (11)$$

Time zone-2:

$$Nu = 1.957 + 0.003Re - 1.0145\phi + 0.014Re\phi \quad (12)$$

Based on the experimental data, friction factor regression equations are proposed for two time zones.

Time zone-1:

$$f = 0.4313 - 0.0007Re + 0.1268\phi - 0.0009Re\phi \quad (13)$$

Time zone-2:

$$f = 0.3781 - 0.0005Re + 0.1145\phi - 0.0007Re\phi \quad (14)$$

3.4. ANN-Support Vector Regression Results

3.4.1. Nusselt Number

The experimentally obtained Nusselt number data is used for the SVR analysis. The Nusselt number is taken as output data, whereas the particle volume loadings and Reynolds number are taken as input data. Usually, among the whole data, some portion of the data is used for the algorithm training, and some portion of the data is used for testing the algorithm. In this case, for the SVR analysis, 70% of the data is used to train the algorithm, and 30% of the data is used to test the algorithm. The performance curve is mentioned in Fig. 11(a), where we can find the best value. Once the iteration has been done in the algorithm, the algorithm will show the best performance value through the mean square error. The best validation performance was observed as 0.0013234 at epoch 30 in this case. Through the output data, the error between the values can be estimated. The error is the difference between target values and output values. Fig. 11(b) represents the error histogram of the Nusselt number. It can be easily observed that the thick pale-yellow line stands for the zero error. Under the best validation, the error of the Nusselt number is obtained as 0.001658 at 20 Bins. Under the best validation performance, the mean square error for the trained data, validation data, and test data are found to be 0.001, 0.0013, and 0.0013, respectively.

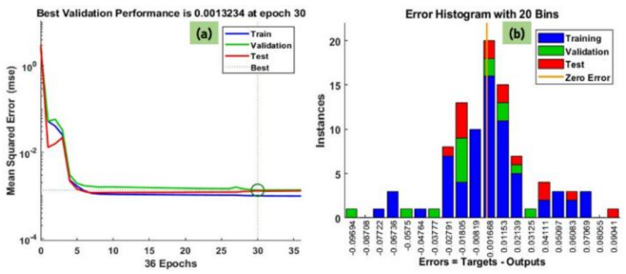

Fig. 11. (a) Performance curve, and (b) error histograms of Nusselt number

The experimental Nusselt number values versus the algorithm output values are plotted like a diagonal plot. Here, we can observe the deviation between the values. In another way, these plots are called as Pearson correlation coefficient (R^2) plots. The Pearson correlations plots are shown in Fig. 12 for the trained data, validation data, test data, and all data. From the figures, the R^2 value is observed as 0.99572, 0.99659, 0.99663, and 0.99487, respectively.

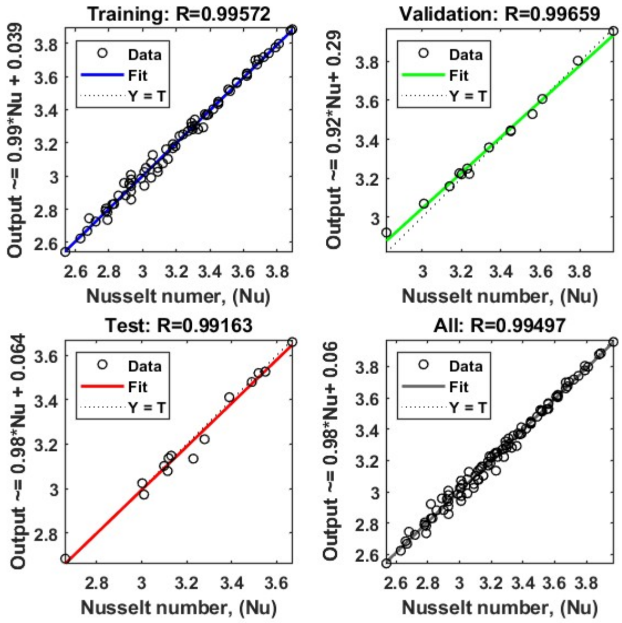

Fig. 12. Correction coefficient of Nusselt number

3.4.2. Heat Transfer Coefficient

The experimentally obtained heat transfer coefficient is used for the SVR analysis. The particle volume loadings and Reynolds number are taken as input data, whereas the heat transfer coefficient is taken as output data. In general, some portion of the data is used for training purposes, and some portion of the data is used for testing purposes in the algorithm. For the present study, SVR analysis, 70% of the data is used for training purposes, and 30% of the data is used for algorithm testing purposes. The performance curve is mentioned in Fig. 13(a), in which we can find the best value. Once the iteration has been done in the algorithm, through the mean square error, the algorithm will show the best performance value. In this case, the best validation performance was observed as 24.6253 at epoch 5. Through the output data, the error between the values can be estimated. The error is the difference between target values and output values. Fig. 13(b) represents the error histogram of the heat transfer coefficient. It can be easily observed that the thick pale-yellow line stands for the zero error. Under the best validation, the error of the Nusselt number is obtained as -0.2588 at 20 Bins. Under the best validation performance, the mean square error for the trained data, validation data, and test data are found to be 10.74, 24.62, and 36.23, respectively.

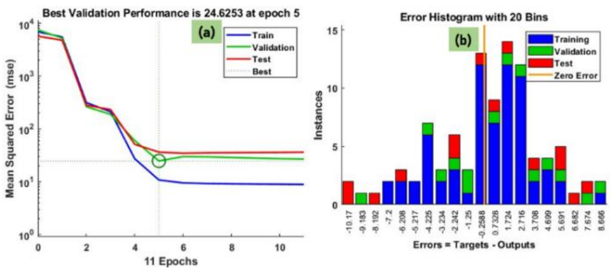

Fig. 13. Performance curve, and (b) error histograms of heat transfer coefficient

The experimental heat transfer coefficient values versus the algorithm output values are plotted like a diagonal plot. Here, we can observe the deviation between the values. The Pearson correlations plots are shown in Fig. 14 for the trained data, validation data, test data, and all data. From the figures, the R^2 value is observed as 0.99674, 0.99262, 0.98439, and 0.9947, respectively.

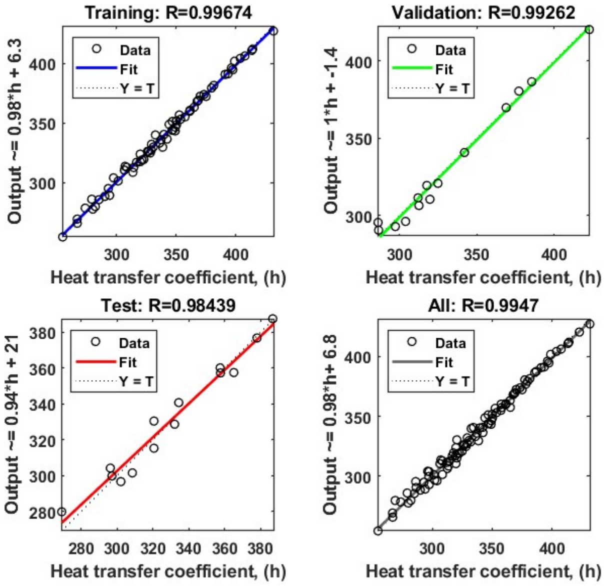

Fig. 14. Correlation coefficient of heat transfer coefficient

3.4.3. Friction Factor

The experimentally obtained friction factor was considered for the SVR analysis. The friction factor is considered as output data, whereas the particle volume loadings and Reynolds number are taken as input data. Usually, among the whole data, some portion of the data is used for the algorithm training, and some portion of the data is used for testing the algorithm. In this case, for the SVR analysis, 70% of the data is used to train the algorithm, and 30% of the data is used to test the algorithm. The performance curve is mentioned in Fig. 15(a), in which we can find the best value. Once the iteration has been done in the algorithm, the algorithm will show the best performance value through the mean square error. In this case, the best validation performance was observed as 6.7447e-08 at epoch 18. Through the output data, the error between the values can be estimated. The error is the difference between target values and output values. Fig. 15(b) represents the error histogram of the friction factor. It can be easily observed that the thick pale-yellow line stands for the zero error. Under the best validation, the error of the friction factor is obtained as 0.000164 at 20 Bins. Under the best validation performance, the mean square error for the trained data, validation data, and test data are found as 1.4054e-6, 6.7447e-6, and 4.3892e-6, respectively.

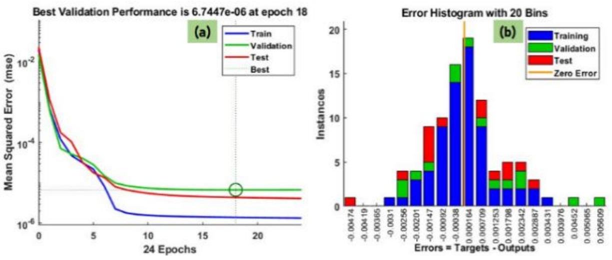

Fig. 15. Performance curve, and (b) error histograms of friction factor

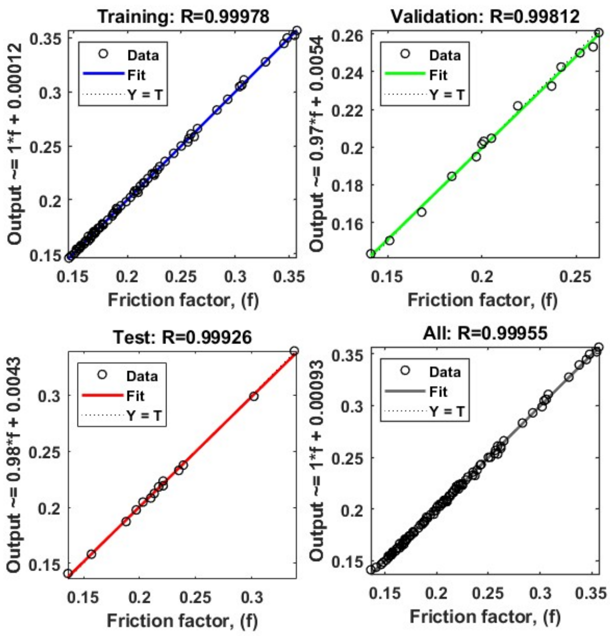

Fig. 16. Correlation coefficient of friction factor

The experimental friction factor values versus the algorithm output values are plotted like a diagonal plot. Here, we can observe the deviation between the values. The Pearson correlations plots are shown in Fig. 16 for the trained data, validation data, test data, and all data. From the figures, the R^2 value is observed as 0.99978, 0.99812, 9.99926, and 0.99955, respectively.

4. CONCLUSION

Experimental studies have been conducted to evaluate the Nusselt number, heat transfer coefficient, and friction factor of FPC working with Al_2O_3-CuO/water hybrid nanofluids. Subsequently, an Artificial Neural Network - Support Vector Regression method was employed to predict the values that were experimentally obtained. The experiments were performed between 09:00 and 16:30 hrs, with volume loadings of 0.048%, 0.096%, 0.144%, 0.192%, and 0.24%, respectively. The time period from 09:00 hr to 16:30 hr was separated into two time zones: time zone 1 (09:00 to 13:00) and time zone 2 (13:00 to 16:30). It is indicated that, at time zone 1, at 13:00 hrs, 0.24% vol. and a Reynolds number of 364.66, the Nusselt number is increased by 20.43%, over the base fluid. Similarly, in time zone 2, at 16:30, with a volume fraction of 0.24% and at a Reynolds number of 211.23, the Nusselt number is increased by 14.08% compared to the base fluid. For the time zone-1, at 13:00 hrs, with 0.24% vol. and a Reynolds number of 364.66, the friction factor is increased by 15.34% over the base fluid. For the time zone-2, at 16:30, at 0.24% vol. and a Reynolds number of 211.23, the friction factor is raised by 11.50% against the base fluid.

In this study, it is noticed that, with the use of hybrid nanofluids in an FPC system, the overall efficiency is enhanced when compared to water in the FPC system. Both the heat transfer coefficient and friction factor are enhanced by using the hybrid nanofluids in an FPC system, but compared to the enhancement of heat transfer, the friction factor enhancement is negligible.

The obtained data is predicted using the ANN-SVR algorithm. The utilised SVR technique effectively predicts the values that closely correspond to the experimental data. The correlation coefficients obtained for the Nusselt number, heat transfer, and friction factor are 0.99497, 0.9947, and 0.99955, respectively.

APPENDIX: UNCERTAINTY ANALYSIS

Uncertainty of the measurements was analysed through the Coleman and Steel [32] procedure. The maximum values of various parameters are mentioned in Table 3.

Table 3. The uncertain values of various parameters

S. No.	Parameter	Maximum values	Uncertainty, (ΔX)
1	d_i	0.006 m	0.00007 m
2	d_o	0.007 m	0.00007 m
3	L	5 m	0.001 m
4	$\dot{m}$	0.0225	3.32×10^{-4} kg/s
5	T_s	89.9	0.1°C
6	T_i	47.5	0.1°C
7	T_o	49.8	0.1°C
8	T_a	40.9	0.1°C
9	T_m	48.65	0.1°C
10	G_T	785	0.03 W/m²
11	ΔP	6.96	0.001 N/m²

Nusselt number

$$\frac{\Delta Q_o}{Q_o} = \left[\left\{\frac{\Delta \dot{m}}{\dot{m}}\right\}^2 + \left\{\frac{\Delta T_o}{T_o}\right\}^2 + \left\{\frac{\Delta T_i}{T_i}\right\}^2\right]^{0.5} \tag{a1}$$

$$\frac{\Delta Q_o}{Q_o} = \left[\left\{\frac{3.32\times10^{-4}}{0.0225}\right\}^2 + \left\{\frac{0.1}{49.8}\right\}^2 + \left\{\frac{0.1}{47.5}\right\}^2\right]^{0.5} = 0.0423 \tag{a2}$$

$$\frac{\Delta Q_o}{Q_o} = [2.187\times10^{-4} + 4.032\times10^{-6} + 4.432\times10^{-6}]^{0.5} \tag{a3}$$

$$\frac{\Delta Q_o}{Q_o} = 0.01501 = 1.501\% \tag{a4}$$

$$\frac{\Delta Nu}{\Delta Nu} = \left[\left(\frac{\Delta h}{h}\right)^2 + \left(\frac{\Delta d_i}{d_i}\right)^2\right]^{0.5} \tag{a5}$$

$$\frac{\Delta h}{h} = A_i\left[\left\{\frac{\Delta Q_o}{Q_o}\right\}^2 + \left\{\frac{\Delta T_w}{T_w}\right\}^2 + \left\{\frac{\Delta T_f}{T_f}\right\}^2 + \left\{\frac{\Delta[ln(d_o/d_i)]}{ln(d_o/d_i)}\right\}^2\right]^{0.5} \tag{a6}$$

$$\frac{\Delta h}{h} = \left[\{0.01501\}^2 + \left\{\frac{0.1}{89.9}\right\}^2 + \left\{\frac{0.1}{48.65}\right\}^2 + \left\{\frac{0.00007}{0.1514}\right\}^2\right]^{0.5} \tag{a7}$$

$$\frac{\Delta h}{h} = [0.0002253 + 1.237\times10^{-6} + 4.225\times10^{-6} + 4.623\times10^{-4}]^{0.5} \tag{a8}$$

$$\frac{\Delta h}{h} = 0.026326 \tag{a9}$$

$$\frac{\Delta Nu}{\Delta Nu} = \left[(0.026326)^2 + \left(\frac{0.00007}{0.01}\right)^2\right]^{0.5} \tag{a10}$$

$$\frac{\Delta Nu}{\Delta Nu} = [0.000691 + 0.000049]^{0.5} = 0.0272 = 2.72\% \tag{a11}$$

Friction factor

$$\frac{\Delta Re}{Re} = \left[\left(\frac{\Delta \dot{m}}{\dot{m}}\right)^2 + \left(\frac{\Delta d_i}{d_i}\right)^2\right]^{0.5} \tag{a12}$$

$$\frac{\Delta Re}{Re} = \left[\left(\frac{3.32\times10^{-4}}{0.0225}\right)^2 + \left(\frac{0.00007}{0.01}\right)^2\right]^{0.5} \tag{a13}$$

$$\frac{\Delta Re}{Re} = [2.187\times10^{-4} + 0.000049]^{0.5} \tag{a14}$$

$$\frac{\Delta Re}{Re} = 0.0162 = 1.62\% \tag{a15}$$

$$\frac{\Delta(\Delta P)}{\Delta P} = \frac{0.001}{6.96} = 1.436\times10^{-4} \tag{a16}$$

$$\frac{\Delta f}{f} = f\left[\left\{\frac{\Delta(\Delta P)}{(\Delta P)}\right\}^2 + \left\{\frac{\Delta L}{L}\right\}^2 + \left\{\frac{3\Delta d_i}{d_i}\right\}^2 + \left\{\frac{2\Delta Re}{Re}\right\}^2\right]^{0.5} \tag{a17}$$

$$\frac{\Delta f}{f} = \left[\{1.436\times10^{-4}\}^2 + \left\{\frac{0.001}{5}\right\}^2 + \left\{3\times\frac{0.00007}{0.01}\right\}^2 + \{2\times0.0162\}^2\right]^{0.5} \tag{a18}$$

$$\frac{\Delta f}{f} = [2.062\times10^{-8} + 4\times10^{-7} + 0.000441 + 0.001049]^{0.5} \tag{a19}$$

$$\frac{\Delta f}{f} = 0.0351 = 3.51\% \tag{a20}$$

CONFLICTS OF INTEREST

The authors declare no conflict of interest.

REFERENCES

[1] A.W. Bhutto, A.A. Bazmib, G. Zahedi, J. Klemes, A review of progress in renewable energy Implementation in the Gulf cooperation council countries. *Journal of Clean Production*, 71, 2014: 168–180. https://doi.org/10.1016/j.jclepro.2013.12.073

[2] S. Jaisankar, T.K. Radhakrishnan, K.N. Sheeba, Experimental studies on heat transfer and friction factor characteristics of forced circulation solar water heater system fitted with helical twisted tapes. *Solar Energy*, 83, 2009: 1943–1952. https://doi.org/10.1016/j.solener.2009.07.006

[3] R.H. Martín, A. García, J. Pérez-García, Influence of wire-coil inserts on the thermo-hydraulic performance of a flat-plate solar collector. *Journal of Physics: Conference Series*, 395, 2012, 012057.

https://doi.org/10.1088/1742-6596/395/1/012057
[4] S.U.S. Choi, Enhancing thermal conductivity of fluids with nanoparticles. *ASME International Mechanical Engineering Congress and Exposition*, *San Francisco, CA*, 1995.
[5] N.B. Ziyadanogullari, H.L. Yucel, C. Yildiz, Thermal performance enhancement of flat-plate solar collectors by means of three different nanofluids. *Thermal Science and Engineering Progress*, 8, 2018: 55–65. https://doi.org/10.1016/j.tsep.2018.07.005
[6] L.S. Sundar, M.K. Singh, A.C.M. Sousa, Experimental investigation of Al_2O_3/water nanofluids on the effectiveness of solar flat-plate collectors with and without twisted tape inserts. *Renewable Energy*, 119, 2018: 820–833. https://doi.org/10.1016/j.renene.2017.10.056
[7] N.S. Rajput, D.D. Shukla, D. Rajput, S.K. Sharma, Performance analysis of flat plate solar collector using Al_2O_3/distilled water nanofluid: An experimental investigation. *Materials Today Proceedings*, 10, 2019: 52–59. https://doi.org/10.1016/j.matpr.2019.02.188
[8] A.A. Hawwash, A.K. Abdel Rahman, S.A. Nada, S. Ookawara, Numerical investigation and experimental verification of performance enhancement of flat plate solar collector using nanofluids. *Applied Thermal Engineering*, 130, 2018: 363–374. https://doi.org/10.1016/j.applthermaleng.2017.11.027
[9] H.J. Jouybari, S. Saedodin, A. Zamzamian, M.E. Nimvari, S. Wongwises, Effects of porous material and nanoparticles on the thermal performance of a flat plate solar collector: An experimental study. *Renewable Energy*, 114, Part B, 2017: 1407–1418. https://doi.org/10.1016/j.renene.2017.07.008
[10] F. Kiliç, T. Menlik, A. Sözen, Effect of titanium dioxide/water nanofluid use on thermal performance of the flat plate solar collector. *Solar Energy*, 164, 2018: 101–108. https://doi.org/10.1016/j.solener.2018.02.002
[11] Z. Said, R. Saidur, N.A. Rahim, Energy and exergy analysis of a flat plate solar collector using different sizes of aluminium oxide based nanofluid. *Journal of Cleaner Production*, 133, 2016: 518–530. https://doi.org/10.1016/j.jclepro.2016.05.178
[12] E.C. Okonkwo, I. Wole-Osho, D. Kavaz, M. Abidb, T. Al-Ansari, Thermodynamic evaluation and optimization of a flat plate collector operating with alumina and iron mono and hybrid nanofluids. *Sustainable Energy Technologies and Assessments*, 37, 2020: 100636. https://doi.org/10.1016/j.seta.2020.100636
[13] S.K. Verma, S.K. Tiwari, A.K. Tiwari, D.S. Chauhan, Performance analysis of hybrid nanofluids in flat plate solar collector as an advanced working fluid. *Solar Energy*, 67, 2018: 231–241. https://doi.org/10.1016/j.solener.2018.04.017
[14] B. Saleh, L.S. Sundar, Thermal efficiency, heat transfer, and friction factor analyses of MWCNT+Fe_3O_4/water hybrid nanofluids in a solar flat plate collector under thermosyphon condition. *Processes*, 9(1), 2021: 180. https://doi.org/10.3390/pr9010180
[15] L.S. Sundar, A.H. Misganaw, M.K. Singh, A.C.M. Sousa, H.M. Ali, Efficiency analysis of thermosyphon solar flat plate collector with low mass concentrations of ND–Co_3O_4 hybrid nanofluids: an experimental study. *Journal of Thermal Analysis and Calorimetry*, 143, 2021: 959–972. https://doi.org/10.1007/s10973-020-10176-1
[16] M.S. Elsherbiny, M. Ali, M. Shahin, M. El-Kady, Experimental study on the effect of micro concentrations of hybrid nanofluids through microchannel heat sinks. *Journal of Applied Computational Mechanics*, 2024: 1–24. https://doi.org/10.22055/jacm.2024.46291.4494
[17] M.S. Elsherbiny, M. Ali, M. Shahin, M. El-Kady, A review of miniature channels and nanofluids technologies used as heat transfer enhancement techniques for microcooling systems. *Journal of Al-Azhar University Engineering Sector,* 19(72), 2024: 185-211. https://doi.org/10.21608/AUEJ.2024.265603.1601
[18] A.M. Ajeena, I. Farkas, P. Vig, Performance enhancement of flat plate solar collector using ZrO_2-SiC/DW hybrid nanofluid: A comprehensive experimental study. *Energy Conversion and Management: X*, 20, 2023: 100458. https://doi.org/10.1016/j.ecmx.2023.100458
[19] M.A. Alfellag, H.M. Kamar, U. Abidin, S.N. Kazi, N.A.C. Sidik, A.S. Muhsan, O.A. Alawi, Optimizing mixing ratio of multi-walled carbon nanotubes and titanium dioxide: A green approach to high-performance hybrid nanofluids for heat transfer. *Powder Technology*, 436, 2024: 119509.

https://doi.org/10.1016/j.powtec.2024.119509

[20] L. Selvam, M. Aruna, I Hossain, R. Venkatesh, M. Karthigairajan, S. Prabagaran, V. Mohanavel, A.H. Seikh, M.A. Kalam, Impact of hybrid nanofluid on thermal behaviour of flat plate solar collector: performance study. *Journal of Thermal Analysis and Calorimetry*, 149, 2024: 5047–5057. https://doi.org/10.1007/s10973-024-12994-z

[21] T. Sathish, J. Giri, R. Saravanan, M. Ubaidullah, S. Shangdiar, S. likela, T. Sithole, K.T.T. Amesho, Amplifying thermal performance of solar flat plate collector by Al_2O_3/Cu/MWCNT/SiO_2 mono and hybrid nanofluid. *Applied Thermal Engineering*, 252, 2024: 123692. https://doi.org/10.1016/j.applthermaleng.2024.123692

[22] L. Xu, A. Khalifeh, A. Khandakar, B. Vaferi, Numerical investigating the effect of Al_2O_3-water nanofluids on the thermal efficiency of flat plate solar collectors. *Energy Reports*, 8, 2022: 6530–6542. https://doi.org/10.1016/j.egyr.2022.05.012

[23] M. Mirzaei, MZ. Mohiabadi, Neural network modeling for accurate prediction of thermal efficiency of a flat plate solar collector working with nanofluids. *International Journal of Ambient Energy*, 42(2), 2021: 227–237. https://doi.org/10.1080/01430750.2018.1525576

[24] Y. Zhang, A. Selamat, Y. Zhang, H. Alrabaiah, A.H. Omar, Artificial neural networks/least squares fuzzy system methods to optimize the performance of a flat-plate solar collector according to the empirical data. *Sustainable Energy Technologies and Assessments*, 52 Part A, 2022: 102062. https://doi.org/10.1016/j.seta.2022.102062

[25] M. Sadeghzadeh, M.H. Ahmadi, M. Kahani, H. Sakhaeinia, H. Chaji, L. Chen, Smart modeling by using artificial intelligent techniques on the thermal performance of flat-plate solar collector using nanofluid. *Energy Science & Engineering*, 7, 2019: 1649–1658. https://doi.org/10.1002/ese3.381

[26] M. Bahiraei, S. Heshmatian, H. Moayedi, Artificial intelligence in the field of nanofluids: A review on applications and potential future directions. *Powder Technology*. 353, 2019: 276–301. https://doi.org/10.1016/j.powtec.2019.05.034

[27] A.M. Tomy, N. Ahammed, M.S.P. Subathra, L.G. Asirvatham, Analysing the performance of a flat plate solar collector with silver/water nanofluid using artificial neural network. *Procedia Computer Science*, 93, 2016: 33–40. https://doi.org/10.1016/j.procs.2016.07.178

[28] L.S. Sundar, Md.H. Farooky, S.N. Sarada, M.K. Singh, Experimental thermal conductivity of ethylene glycol and water mixture based low volume concentration of Al_2O_3 and CuO nanofluids. *International Journal of Heat and Mass Transfer*, 41, 2013: 41–46. https://doi.org/10.1016/j.icheatmasstransfer.2012.11.004

[29] V. Vapnik, The Support Vector Method of Function Estimation. *In: Suykens, J.A.K., Vandewalle, J. (eds) Nonlinear Modeling. Springer, Boston, MA*. 1998. https://doi.org/10.1007/978-1-4615-5703-6_3

[30] C. Cortes, V. Vapnik, Support-vector networks, *Machine Learning*, 20, 1995: 273–297. https://doi.org/10.1007/bf00994018

[31] J.A.K. Suykens, J. Vandewalle, Least square support vector machine classifier. *Neural Processing Letters*, 9, 1999: 293-300. https://doi.org/10.1023/A:1018628609742

[32] H.W. Coleman, W.G. Steel, Experimental and uncertainty analysis for engineers. *Wiley Interscience*, *New York,* 1989.